Inorganic Chemistry Communications 155 (2023) 111057

Contents lists available at ScienceDirect

Inorganic Chemistry Communications

journal homepage: www.elsevier.com/locate/inoche

Short communication

Synthesis, characterization, crystallographic aspects, Fukui function, and photodynamic antifungal chemotherapy investigation of Cd (II)-tricyanomethanide coordination polymer: Insights from DFT

Dhrubajyoti Majumdar [a,*], Jessica Elizabeth Philip [b], Burak Tüzün [c], Sourav Roy [d]

[a] Department of Chemistry, Tamralipta Mahavidyalaya, Tamluk 721636, West Bengal, India
[b] Department of Chemistry, Alphonsa College, Palai, Kottayam, Kerala 686574, India
[c] Sivas Cumhuriyet University, Sivas Vocational School, Department of Plant and Animal Production, TR-58140 Sivas, Turkey
[d] Solid State and Structural Chemistry Unit, Indian Institute of Science, Bangalore 560 012, India

ARTICLE INFO

Keywords:
Antifungal
Cadmium
DFT
TCM
Molecular docking
PLIP
PACT

ABSTRACT

This study delves into the synthesis, crystal structure, structural topology, photodynamic antifungal therapy (PACT), and DFT-based investigations of one $[Cd(TCM)_2]_n$ coordination polymer (TCM = tricyanomethanide). The complex was structurally characterized using elemental, IR/Raman, UV–Visible spectroscopy, PXRD, EDX-SEM, and X-ray diffraction. X-ray structure divulges that the complex crystallizes in the orthorhombic space group Pmna where Cd(II) centres assume octahedral geometry and are coordinated by six N atoms from six TCM. The topology analysis reveals an sqc8 topology with Cd(II) occupying the nodes, where the TCM connectors form edges. The crystal packing consists of unique nitrile···nitrile interactions at 3.276 Å. The crystal packing is confirmed by Hirshfeld surface (HS) and 2D fingerprint plots. The Cd···N contact makes up 35.1% of the packing, while the C···C and N···N contacts contribute 21.2% and 20.6%, respectively. The complex DFT optimization was contrived in B3LYP, HF, and M06-2x methods employing the 3–21 g, lanl2dz, and sto-3 g level of basis sets. Here chemical reactivity is supported by the HOMO-LUMO energy gap and ESP. The electrophilic (E +) and nucleophilic (Nu^-) sites were examined by Fukui function values (f_x^+, f_x *and* f^0). The NLO parameters support the complex optical properties. The molecular docking simulation (MD) and protein–ligand interactions profiler (PLIP) has shown promising results in studying the relationship between complex and cancer proteins at a biological level. The article vivdly discusses the photodynamic antifungal therapy's effectiveness using MIC value against antibiotic-resistant strains when used with complex, TCM, and metal salts. The most effective mechanisms include membrane disruption, ROS, and cell cycle arrest.

1. Introduction

The trending pseudohalides chemistry in coordination chemistry gains constant importance, especially for synthetic inorganic chemists [1,2]. Researchers worldwide are involved in their research effort to explore new avenue in crystal engineering to develop novel properties of crystal complexes beneficial to the human being or industry as coordination complexes crystal engineering is a rapidly expanding research field [3]. Based on this, one exciting pseudohalide, potassium tricyanomethanide $[KC(CN)_3]$ (TCM), was first discovered in 1896 by Schmidtmann [4] to expand crystal engineering. Consistent with the previous pseudohalide concept [4,5], several research works explore that [NCO]-, $[C(CN)_3]^-$ and $[N(CN)_2]^-$ are very similar species possessing an ambident binding ability that a rarely observed Group IV/V pairs of donor atoms (Scheme S1) [5]. Scheme S1 divulges the TCM electronic arrangement and bridging actions that are parallelism with $[N(CN)_2]^-$ [4]. Notably, examples of C/N bonding, ionic bonding, and bridging have been reported vividly [5]. Riveting the systematic exploration of TCM as a ligand in coordination chemistry only began 30 years ago. Kohler et al. published remarkable works on transition metal compounds with these pseudohalides [6]. Moreover, TCM is a versatile three-connecting building block employed for universal coordination networks in self-assembly [7–11]. They often behave like μ1 or μ3-bridges connecting two or three M−centres to create extended 1D/2D/3D aggregates [9]. The bridging assembly M—N≡C—N≡N—M^1, M—N≡C—C(CN)— C≡N—M^1 is nonlinear due to sp^2 hybridization of

* Corresponding author.
E-mail address: dmajumdar30@gmail.com (D. Majumdar).

https://doi.org/10.1016/j.inoche.2023.111057
Received 21 May 2023; Received in revised form 26 June 2023; Accepted 8 July 2023
Available online 19 July 2023

the central N/C atom with an M…M[1] separation of more than 7.5 Å [9]. Under this circumstance, the coordination complexes building blocks constructed from TCM have sparked significant interest due to their fabulous structural motifs and novel properties belonging to their optical, magnetic, and electronic [12]. Besides, the quasi-pi conjugated TCM is an effective mediator for transmitting magnetic and electronic interactions [12]. Further, scientists have perceived that coordination chemistry research has been expanded by utilizing DFT-based studies like HSA, MEP, Fukui function, NLO, and HOMO-LUMO. Meanwhile, HSA thoroughly analyzed the crystal structure supramolecular interactions of various cadmium complexes and coordination polymers [13,14]. DFT also explains metal complexes' chemical reactivity [15,16], topology, optical, and selectivity in the local hard-soft acid-base (HSAB) theory. Because of this, numerous studies [17–19] demonstrate that the HSAB principle is frequently applied to examine the site selectivity in a molecule. Concerning DFT computations, soft–soft interactions are preferred at the maximum. Fukui function zone, whereas hard-hard interactions are selected in the minimum Fukui function region [20,21]. Electrophile and nucleophile regions were determined by calculating the Fukui function of the metal complex. Herein, the DFT calculations of the metal complex were made in B3LYP, HF, and M06-2x [22–24] methods with the 3–21 g, lanl2dz, and sto-3 g basis sets. Meanwhile, the quantum chemical studies concerning the antimicrobial potency of the complex were conducted using MD and PLIP experiments. The studies are becoming more attractive because various cadmium complexes and coordination polymers have shown the potential to address antimicrobial issues [14,25,26]. These studied against cancer proteins that are breast cancer protein (PDB ID: 1JNX) [27], lung cancer protein (PDB ID: 2H80) [28], liver cancer protein (PDB ID: 3WZE) [29], and colon cancer protein (PDB ID: 4UYA) [30]. Interestingly, the research of photodynamic antifungal therapy (PACT) has drawn tremendous interest from the scientific society since it is a special treatment that uses light-sensitive drugs. It is for its practical potential function to kill multidrug-resistant pathogenic bacteria. Also, here a light source is used in this treatment to destroy abnormal cells. It can be used in various medical fields, including antimicrobial therapy, cancer treatment [31–34], ophthalmology, and even acne. PACT can effectively destroy microbes like bacteria, fungi, and viruses [35–38]. The heavy burden of fungal infections, and the increase in fungal strains resistant to the current antifungals globally, have rendered the development of new therapeutic strategies, such as antifungal photodynamic therapy, an urgent requirement.

In this context, our research focuses on the synthesis, characterization, structural topology, and crystal structure of one new Cd(II)-based coordination polymer featuring TCM connecting building blocks. In the meantime, DFT-based studies of the Fukui function, HOMO-LUMO, ESP, NLO parameters, and HSA provide evidence for complex areas of electrophilicity/nucleophilicity, reactivity, optical activities, and supramolecular interactions. We conducted MD and PLIP experiments to understand better the biological relationship between metal complexes and cancer proteins. Ultimately, we paid close attention to the mechanistic details of photodynamic antifungal therapy against antibiotic-resistant strains using MIC values to compare the effectiveness of the complex, TCM, and metal salts.

2. Experimental

2.1. Materials and instrumentation

All the research chemicals and solvents were purchased from Aldrich, Sigma, USA, Company and used as received without further purification. The purity of $Cd(OAc)_2{\cdot}2H_2O$ is (99%), Sodium tricyanomethanide (TCM) (Na^+ $^-C(CN)_3$) (98%), Methanol (99.9%), and Dichloromethane (DCM) (99.9%). The standard C and N elements were analyzed using a PerkinElmer 2400 (CHN Elemental) Analyzer. FT-IR spectra were recorded in solid KBr pellets (4000–400 cm^{-1}). It employed the 16 scans at a wavenumber resolution of 4 cm^{-1} on a PerkinElmer spectrum RX 1 and the DTGS (deuterated triglycine sulfate) detector. Raman spectra were recorded using the BRUKER RFS 27 model (4000–50 cm^{-1}). PXRD measurements were successfully conducted using the BRUKER AXS model with Cu K radiation from the GERMANY X-ray diffractometer D8 FOCUS.SEM micrographs were analyzed using the JEOL model JSM6390LV, and the EDX was performed on the EDX OXFORD XMX N with a W filament. UV–Visible spectra (200–1100 nm) in DCM solvent were determined with the Hitachi model U-3501 spectrophotometer.

2.2. Synthesis and crystallization of $[Cd(TCM)_2]_n$

$Cd(OAc)_2{\cdot}2H_2O$ (0.267 g, 1 mmol) and the Sodium tricyanomethanide (TCM) (0.113 g, 1 mmol) were dissolved in a hot 35 mL methanol with continuous stirring under a magnetic stirrer for about 1 h. The temperature of the reaction mixture was adjusted to 75 °C. In the meantime, we added ten drops of hot dichloromethane (DCM). The resultant mixture was further refluxed at room temperature for 2 h. The light-yellow solution was filtered and refrigerated for crystallization at room temperature by slow evaporation. After 15 days of spending, plate-sized, light, yellow-coloured single crystals were obtained, suitable for SCXRD. Crystals were isolated by filtration, washed with dry ether, and air-dried. Yield: 0.421 g, (51%), Anal. Calc. for C_8CdN_6: C, 32.85; N, 28.73. Found: C, 32.79; N, 28.68 %. IR (KBr) (cm^{-1}) selected bands: free TCM, ν(CN) 2179 cm^{-1}, TCM in complex, ν(CN) 2204 cm^{-1}, 2277 cm^{-1}, Raman (cm^{-1}) selected band for complex: ν(CN) 2202 cm^{-1}, 2270 cm^{-1}, Complex, UV–Vis λ_{max} (DMF): 280 nm, free TCM, UV–Vis λ_{max} (CH_3OH): 234, and 270 nm.

2.3. X-ray crystallography

Light-yellow cadmium crystal complex was developed after several days of evaporating methanol and DCM medium's mixed solvent. To process crystal data, we carefully selected 3 to 5 high-quality crystals and observed them microscopically. Crystals were collected on a Bruker CCD [39] diffractometer using Mo Kα radiation at room temperature (=0.71073 Å). When collecting crystal data, we utilized multiple crystallographic programs that are commonly used. For example, SMART is used for accumulating frames of information, indexing reflections, and determining lattice parameters, SAINT [40] for combining the intensity of reflections and scaling, SADAB [41] for absorption correction, and SHELXTL for determining space groups and structures, as well as least squares refinements on F^2. The crystal structure was entirely solved by full-matrix least-squares methods against F^2 using SHELXL-2014 [42] and Olex-2 software [43]. A summary of the crystallographic information and structure refinement parameters is shown in Table 1.

2.4. Computational methodology

Theoretical DFT calculations provide essential information about molecules' chemical and biological properties [44]. Therefore, many quanta chemical parameters are obtained from theoretical calculations. The calculated parameters are used to explain the vital chemical activities of the molecules. Many programs are used to calculate molecules. These programs are Gaussian09 RevD.01 and Gauss View 6.0 [45,46]. These programs considered calculations in B3LYP, HF, and M06-2x [22–24] methods with the 3–21 g, lanl2dz, and sto-3 g basis sets. As a result of these calculations, many quanta chemical parameters have been found. Each parameter describes a different chemical property of molecules. The calculated parameters are calculated as follows [47].

$$\chi = -\left(\frac{\partial E}{\partial N}\right)_{v(r)} = \frac{1}{2}(I+A) \cong -\frac{1}{2}(E_{HOMO}+E_{LUMO})$$

Table 1
Crystal data and full structure refinement parameters.

Empirical formula	C_8CdN_6
Formula weight	292.55
Temperature/K	293(2)
Crystal system	orthorhombic
Space group	*P*mna
a/Å	7.802(3)
b/Å	5.467(2)
c/Å	10.726(4)
α/°	90
β/°	90
γ/°	90
Volume/Å^3	457.5(3)
Z	2
ρ_{calc}g/cm^3	2.124
μ/mm^{-1}	2.356
F(000)	276.0
Crystal size/mm^3	0.300 × 0.200 × 0.100
Radiation	MoKα (λ = 0.71073)
2Θ range for data collection/°	6.458 to 56.694
Index ranges	$-10 \le h \le 10$, $-7 \le k \le 7$, $-14 \le l \le 14$
Reflections collected	9216
Independent reflections	618 [R_{int} = 0.0345, R_{sigma} = 0.0129]
Data/restraints/parameters	618/0/42
Goodness-of-fit on F^2	1.341
Final R indexes [I>=2σ (I)]	R_1 = 0.0197, wR_2 = 0.0497
Final R indexes [all data]	R_1 = 0.0208, wR_2 = 0.0508
Largest diff. peak/hole / e Å^{-3}	0.42/-1.36

$$\eta = -\left(\frac{\partial^2 E}{\partial N^2}\right)_{v(r)} = \frac{1}{2}(I-A) \cong -\frac{1}{2}(E_{HOMO} - E_{LUMO})$$

$$\sigma = 1/\eta\omega = \chi^2/2\eta\varepsilon = 1/\omega$$

Fukui functions can be expressed using the difference approximation, as follows:

$$f_x^+ = q_{(N+1)} - q_{(N)}$$

$$f_x^- = q_{(N)} - q_{(N-1)}$$

where $q_{(N+1)}$, $q_{(N)}$, and $q_{(N-1)}$ are Mullikan charge of the atom with N + 1, N, and N-1 electrons.

A technique exists for contrasting the metal complexes' biological actions with protein ones. Molecular docking is one of the most typical of them. Metal complexes can be compared using a few of these molecular docking techniques. The HEX software is employed in this investigation. These enzyme proteins interact with the ligand and its metal complexes to boost their biological activity [48]. Molecules' biological activities were compared to those of enzymes using molecular docking calculations. At HEX 8.0.0, the enzyme and molecule files were examined [49]. For docking, the following variables are used: Correlation type shape only, 3D FFT mode, 0.6-dimensional grid, 180-degree receptor, ligand ranges, 360-degree twist range, and 40-degree distance range. The interaction between the compounds and the proteins was also thoroughly examined using the Protein-Ligand Interaction Profiler (PLIP) service [50,51]. Hirshfeld surfaces [52–54] and two-dimensional fingerprint plots [55,56] have been calculated using Crystal Explorer [57] software. d_e and d_i are defined for each point on the Hirshfeld surface to calculate the normalized contact distance (d_{norm}) using the appropriate formula. The d_{norm} value depends on the relative importance of intermolecular contacts and van der Waals separations. The Hirshfeld surface with a red-white-blue colour scheme is displayed with the d_{norm} parameter. The bright red spots indicate shorter connections. White areas represent contacts around the van der Waals separation, and blue regions, conversely, signify the absence of any close contacts.

2.5. Agar well diffusion method

Petri plates containing 20 mL Mueller Hinton medium were seeded with a 24 h culture of fungal strains. Wells of diameter 6–8 mm were cut aseptically with a sterile cork borer into which 20 μL of the sample dispersion of desired concentration was introduced. The plates were then successfully incubated at 37 °C for 24 h. The antifungal function was then evaluated by measuring the diameter of the inhibition zone developed around the well. Minimum inhibitory concentration (MIC): broth microdilution method: An antimicrobial agent's MIC is defined as its lowest concentration that can result in visible inhibition of microbial growth. It also establishes the level of microbial resistance to an antimicrobial agent. The broth microdilution method determined the minimum inhibitory concentration (MIC). 50 μg/mL of the sample solution in twofold dilutions (2 μg/mL, 4 μg/mL, 8 μg/mL, 16 μg/mL, and 32 μg /mL) were prepared in broth medium using a 96-well microtitration plate. Each well is then inoculated with 50 μL of the microbial inoculum prepared in the same growth medium after dilution to 0.5 McFarland scale. After well-mixing, the inoculated wells were incubated for 18 h at 37 °C. MIC was taken as the lowest concentration that causes a visible inhibition of fungal growth which is indicated by the absence of turbidity with the addition of the antimicrobial solution. CLSI (Clinical and Laboratory Standards Institute) has standardized the broth dilution protocol for fungi.

2.6. Time-kill kinetics

Time-kill kinetic study of compounds was investigated to determine the antifungal efficiency. After being incubated in 4 mL TSB medium overnight at 37 °C while shaking, 100 μL fungal solution was transferred into 4 mL fresh medium to incubate for 6 h at the same condition to obtain the mid-log phase fungal. Fungal suspensions (106 CFU/mL) were made and then incubated with different concentrations of samples at 37 °C for 10 min, 30 min, 60 min, and 120 min, respectively. The fungal suspensions and sample mixture were diluted 102 -fold and then spread on the TSB agar plates then diluted 104-fold. These plates were incubated preferentially at 37 °C for 20 h [58]. The number of colonies on each plate was counted and plotted against the incubation time, and the experiment was repeated three times.

3. Results and discussion

3.1. Synthetic perspective

The cadmium complex was synthesized in a 1:1 M ratio using in situ self-assembly method (Scheme 1). The complex obtained a moderately good yield from cadmium acetate dihydrate and TCM linker in methanol and DCM mixed solvent medium. The complex is insoluble in water and soluble in most common organic solvents like DMSO, Ether, DMF, etc. The complex was characterized using IR, Raman, UV–Visible spectra, PXRD, SEM-EDX, and single-crystal X-ray diffraction study. Moreover, the elemental composition was supported by the EDX analysis separately for TCM and the complex. The EDX profiles show that TCM acts as a ligand with cadmium metal, revealing distinct components. The different SEM morphology of TCM and the complex further justified the complexing nature of TCM [59]. Notably, TCM is a versatile three-connecting building block employed for universal coordination networks in self-assembly. It thus synthesizes various metal complexes [7–11]. We ensure in the current research that HSA/MD/PLIP/time-kill kinetics-like experiments, topological analysis, the Fukui function values, and the NLO parameters support the electrophilic/nucleophilic regions, and the optical modulation all are positively unveiled in the literature. In addition, the investigation of photodynamic antifungal therapy against antibiotic-resistant strains creates a new opportunity, especially for researchers in the crystal engineering field. Therefore, today the coordination chemistry branch of TCM has become an

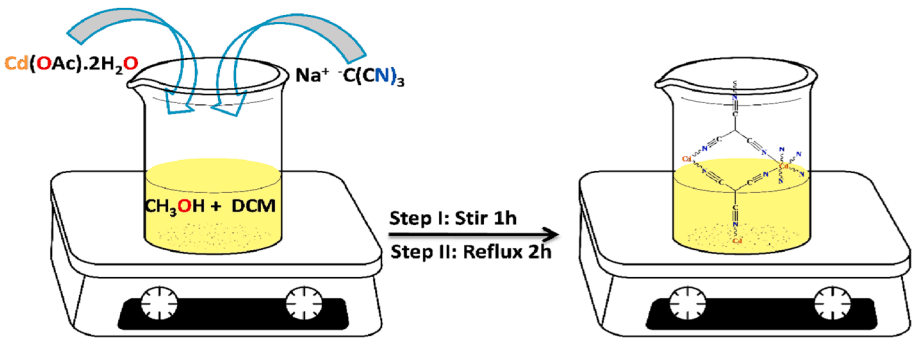

Scheme 1. Synthetic outline for the cadmium complex.

intriguing research interest to synthetic chemists.

3.2. Characterization

3.2.1. FT-IR

Structural characterization of newly synthesized compounds is becoming increasingly crucial for all synthetic chemists. Therefore, we priority basis characterized the synthesized complex by IR analysis. Herein we discuss the IR spectral feature for free TCM ligands and the coordinated TCM comparatively. The coordination binding modes of $[C(CN)_3]^-$ are frequently determined using IR spectral analysis where the v(CN) vibration is of prime importance (Scheme S1) [4]. Notably, the spectra of the free ions show strong v(CN) bands at 2179 cm^{-1} for free $[C(CN)_3]^-$ cm^{-1} [4]. In the IR spectra of tricyanomethanide complexes with N-coordinated $[C(CN)_3]^-$ two or three v(CN) bands around 2230 and 2175 cm^{-1} are frequently observed (Scheme S1) [4]. In the case of C-coordination, two v(CN) bands should appear in the same range [4]. Therefore, we have observed a different category of strong IR band when co-ligand TCM is joined with Cd(II) metal ions near 2204 cm^{-1} (Fig.S1). Besides, the distinct IR band's shift value of 2277 cm^{-1} supports the tridentate bonding feature of $[C(CN)_3]^-$ with cadmium metal ions (Scheme S1 VIII) [4,11,12]. Hence, the comparative IR spectral approach (TCM vs. complex) ensures that the TCM is a potential linker towards cadmium metal ions.

3.2.2. Raman spectra

We have also characterized the complex using Raman spectra. The Raman peak 2202 cm^{-1} in the complex further confirms the TCM is linked with the cadmium metal ions (Fig.S2). Besides, the significant Raman's band's shift value of 2270 cm^{-1} ensures the tridentate binding of $[C(CN)_3]^-$ with cadmium metal ions (Scheme S1 VIII) [4].

3.2.3. UV–Visible spectra

We have also characterized the complex employing the UV–Visible spectral study. We have taken UV–Visible spectra in methanol for TCM and the complex for DMF solvent (Fig.S3). The spectral ranges show that TCM prominent peaks arise at 234 nm and 270 nm, respectively, whereas complex UV spectral major peaks observe at 280 nm. The result indicates that this type of electronic transition is due to M → LCT (Metal to Ligand) charge transfer. The enhancement of spectra is due to when TCM has coordinated with cadmium metal ions and thereby increased the M → LCT process. The π-accepting ligand, tricyanomethanide, can raise the emission energy. Several TCM complexes exhibit similar UV–Visible spectral behaviour [12].

3.2.4. EDX-SEM

EDX is a popular X-ray technique used to identify the elemental composition of synthesized complex materials. The EDX-generated data consists of several spectra divulging peaks corresponding to the elements, and the analysis is made up of the accurate composition of the analyzed sample. By using the EDX technique on both TCM and complex separately, we could distinguish the chemical composition of Cd as metal ions. It is because the EDX profiles differ between the two. The study further ensures the interaction between TCM and cadmium metal salts [59]. Aside from that, C and N are the only elemental compositions from the TCM linker (Table S2 and Fig.S4). Again, a scanning electron microscope (SEM) is used to study the morphology of as-synthesized materials. It generates different images of a ready mix employing scanning the surface with a focused beam of electrons. The electrons interact with the sample atom and generate various signals containing information about the surface topography, size, and morphological structure. We performed an SEM experiment with TCM and the complex separately to determine the changes in morphology, primarily when TCM acts as a potential linker. The SEM images of the TCM and complex are shown in ESI-2 and ESI-3. The SEM profiles of TCM are flower-type plate shape, but when it is linked with cadmium metal ions, morphology changes as ice types. The SEM figures compare the linking behaviour of TCM and cadmium metal ions [59].

3.2.5. Powder X-ray diffraction

We further characterized the prepared complex phase purity and crystallinity by the PXRD analysis. Here the PXRD experiment recorded diffraction patterns at room temperature. Experimentally the compound scanning in the range ($2\theta = 40–50^0$) and thus recorded the PXRD patterns. The complex, well-defined individual sharp PXRD peaks support the crystalline nature (Fig.S5). Herein the complex's experimental and simulated PXRD patterns (obtained from the cif file from Mercury Software) match well, indicating the consistency of the bulk sample i.e. cadmium complex.

4. Crystal structure description

The X-ray crystal structure determination revealed that complex crystallizes in the orthorhombic space group *Pmna* with cell parameters a = 7.802(3), b = 5.467(2), c = 10.726(4)Å, V = 457.5(3) $Å^3$, and Z = 2. The complex is a coordination polymer composed of infinite two-dimensional sheets forming a rutile-like framework where the cadmium centres are linked by bridging TCM anions. The distance between the 3- and 6-connecting nodes in the rutile prototype (TiO_2) is the same as the Ti-O distance, which is 1.946(3) and 1.984(4) Å. On the other hand, in the complex, the separation between these nodes is more extensive, which is around 4.5–5.0 Å and is determined by the C—C—N—Cd distance. The outcome is a spacious structure that permits a second framework to interweave with the first, as illustrated in Fig. 2. It is worth noting that the $M(dca)_2$ compounds possess a single rutile-like network. Within this network, connections between 3- and 6-connecting nodes resemble the C—C—N—M connections found in the $M(TCM)_2$ derivatives, as they share a similar length and belong to the N-C-N-M type [60]. Details of the crystallographic data are given in Table 1. The perspective view of the complex is shown in Fig. 1. The TCM ligand is bridging with three cadmium (II) centres. In contrast, the cadmium (II) centres are coordinated by six nitrogen atoms from six tricyanomethane

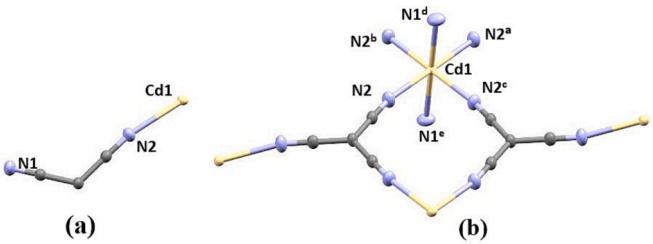

Fig.1. Perspective view of complex (b), and asymmetric unit (a). [a]=1-x,2-y,1-z; [b]=1-x, y, z; [c]=x,2-y,1-z; [d]=1/2 + x,1 + y,3/2-z; [e]=1/2-x,1-y, −1/2 + z.

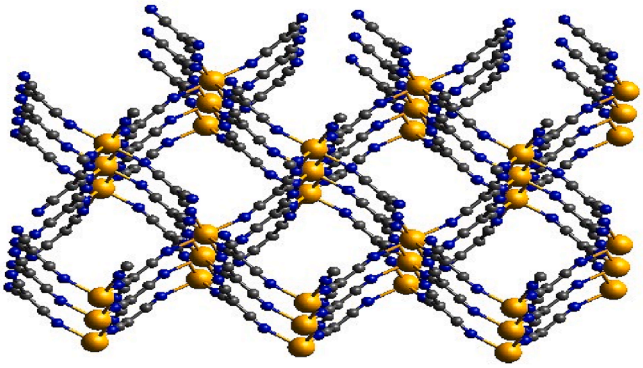

Fig.2. Crystal packing of complex (along the b axis).

ligands. Among them five are symmetry-related [N(1)^{e}, N(2)^{a}, N(2)^{b}, N(1)^{d}, N(2)^{c}] a = 1-x,2-y,1-z; b = 1-x,y,z; c = x,2-y,1-z; d = 1/2 + x,1 + y,3/2-z; e = 1/2-x,1-y,-1/2 + z, resulting in an octahedral geometry. The Cd-N bond distances in the axial sites are longer (2.355 Å) compared to the Cd—N bond distances (2.308 Å) in the equatorial sites. The N-Cd-N angles vary from 88.87° to 180°. The N—Cd—N angles vary from 88.87° to 180°. The bond distances and angles are closely connected to the published analogous complexes [7–11].

4.1. Supramolecular interactions

We have explored in detail the crystal supramolecular interactions. A perspective view of the crystal packing is shown in Fig. 2. The crystal packing mainly consists of unique nitrile···nitrile interactions at 3.276 Å (Fig. 3), which is very uncommon in the literature published analogous complexes [7–11]. But recently, comparable interactions have been vividly observed in a few complexes [59].

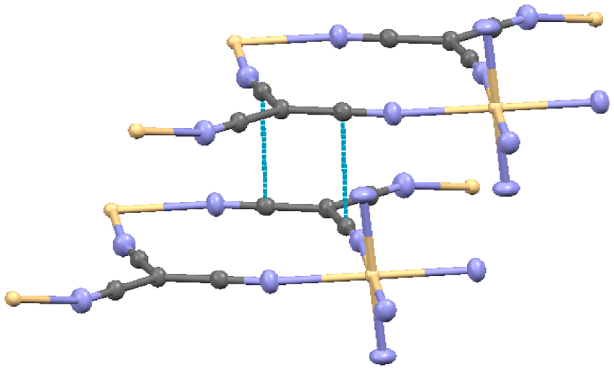

Fig.3. Nitrile···nitrile interactions in complex.

4.2. Topological approach

This complex, interesting topology analysis reveals an sqc8 topology (Fig. 4) with Cd(II) occupying the nodes, where the tricyanomethanide connectors form edges. Such topological feature is absent in the literature published analogous complexes [7–11].

5. Density functional theory

5.1. Hirshfeld surface

Analysis from the mercury software reveals that the complex has several contacts and supramolecular interactions, which are further studied by Hirshfeld surface analysis (HSA). HSA provides an overall understanding of the electronic distribution over the complex. HS of the complex have been mapped over d_{norm} (−0.5 to 1.5 Å), shape index (−1.0 to 1.0 Å), and curvedness (−4.0 to 0.4 Å) as shown in Fig. 5. The red patches observed in d_{norm} represent interactions or contacts. M···N, N···N, and C···C interactions/contacts are largely detected. 2D fingerprint plots recognized from d_e and d_i, explain the contribution of the observed contacts/interactions in the complex (Fig. 5). The Cd···N contact is found to be 35.1% while the C···C and N···N contacts are contributing 21.2% and 20.6% respectively to the overall contacts established in the complex. The C···N contact is found to be 23% which also supports the nitrile···nitrile contact observed in the crystal packing. This C···N/N···C interaction also appears as distinct spikes in the 2D fingerprint plots (Fig. 5). The lower spike corresponding to the donor spike represents the C···N interactions (d_i = 1.8, d_e = 1.6 Å) and the upper spike being an acceptor spike represents the N···C interactions (d_i = 1.6, d_e = 1.8 Å) in the fingerprint plot (Fig. 5). The Cd···N interaction also appears as two distinct spikes in the 2D fingerprint plots (Fig. 5). The lower spike corresponding to the donor spike represents the Cd···N interactions (d_i = 1.3, d_e = 1.1 Å) and the upper spike being an acceptor spike represents the N···Cd interactions (d_i = 1.1, d_e = 1.3 Å) in the fingerprint plot (Fig. 5). The N···N interaction appears as two distinct spikes in the 2D fingerprint plots (Fig. 5). The lower spike corresponding to the donor spike represents the N···N interactions (d_i = 1.7, d_e = 1.3 Å) and the upper spike being an acceptor spike represents the N···N interactions (d_i = 1.3, d_e = 1.7 Å) in the fingerprint plot (Fig. 5). Unlike other interactions, C···C interactions show only one spike with (d_i = 0.7, d_e = 0.7 Å).

5.2. HOMO-LUMO

Theoretical calculations are an essential method used quickly and efficiently when comparing the activities of molecules. First, many quanta chemical parameters are calculated due to Gaussian calculations (Table 2). Each of these estimated parameters explains many different properties of molecules and provides information about molecules with these properties. Among these parameters, two essential parameters allow the activities of molecules to be compared: the HOMO and LUMO parameters of the molecules. The first of these parameters, the HOMO parameter of molecules, shows the ability of molecules to donate electrons. The molecule with the most positive numerical value of this parameter has the highest activity [61]. The other parameter, which is the second of these parameters, is the molecules' LUMO. This parameter's numerical value indicates the electron-accepting ability of the molecules, and the numerical value of the molecule with the most negative value has the higher activity [62].

Apart from these parameters, another calculated parameter is the ΔE parameter, which is known to have high activity if the numerical value of this parameter is low [61]. The low value of this value facilitates electron transfer. Another parameter is electronegativity, which is the power of each of the atoms forming a bond to attract bond electrons; the numerical value of this parameter is known to have the highest activity of the smallest molecule [62]. Many properties of molecules are

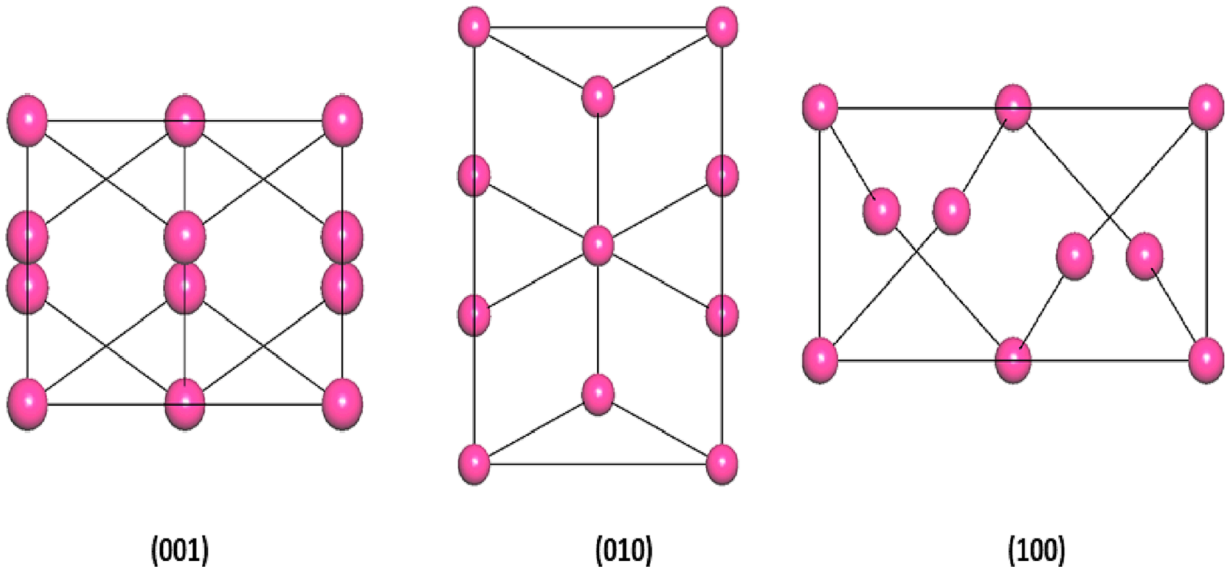

Fig.4. A perspective view of sqc8 topology in different planes of complex.

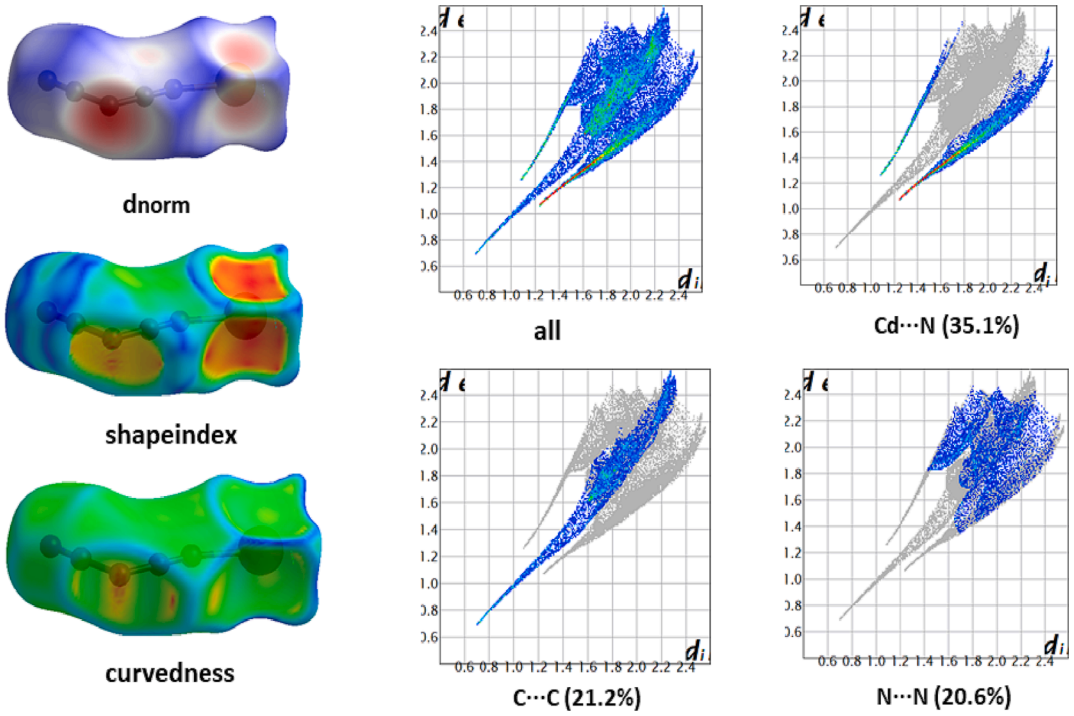

Fig.5. A-b Hirshfeld surfaces and different contacts in the complex.

examined with the calculations made. Another calculated parameter is chemical hardness and softness, which are essential parameters that express the measure of reactivity and stability [62]. Softness, which is the opposite of chemical hardness (1/η), describes the polarization property of molecules. Soft molecules are more reactive than hard molecules as they readily offer electrons to an acceptor molecule.

Although many parameters have been obtained from the calculations, few of the obtained parameters have visual representations. The parameters obtained from the visuals are given in Fig. 6. Here, the optimized structures of molecules are given in the first image. The second and third images show the locations of the HOMO and LUMO orbitals of the molecules. The last image is the molecular electrostatic potential map (ESP) of the molecule. In this image, the red-coloured regions are the regions with the highest electron density [63]. However, the blue-coloured areas have the lowest electron density [61].

5.3. *Fukui function*

Typically, the greatest f_x^- or f_x^+ value will indicate the favoured location for assault by electrophilic (E^+) and nucleophilic (Nu^-) agents. From the perspective of the e-simple molecular orbital theory model, all known theories suggest that more electrons are added to the lowest unoccupied molecular orbital (LUMO). In contrast, electrons are removed from the highest occupied molecular orbital (HOMO) during ionization [64,65]. In the Fukui function technique and are therefore anticipated to be related to LUMO and HOMO, respectively (Table 3).

Table 2
The calculated quantum chemical parameters of complex.

E_{HOMO}	E_{LUMO}	I	A	ΔE	η	μ	χ	Pİ	ω	ε	Dipole	Energy
B3LYP/3–21 g LEVEL												
−5.0641	−0.6808	5.0641	0.6808	4.3832	2.1916	0.4563	2.872	−2.8725	1.8824	0.5312	5.1394	−154193.538
B3LYP/6–31 g LEVEL												
−5.5395	−0.8738	5.5395	0.8738	4.6657	2.3329	0.4287	3.206	−3.2066	2.2038	0.4538	4.3294	−7428.851
B3LYP/SDD LEVEL												
−2.0972	1.7709	2.0972	−1.7709	3.8681	1.9341	0.5170	0.163	−0.1631	0.0069	145.34	1.0700	−153353.854
HF/3–21 g LEVEL												
−6.6565	14.4031	6.6565	−14.403	21.0596	10.529	0.0950	−3.873	3.8733	0.7124	1.4037	4.5056	−154087.668
HF/6–31 g LEVEL												
−7.3379	1.5331	7.3379	−1.5331	8.8710	4.4355	0.2255	2.902	−2.9024	0.9496	1.0531	4.4121	−7350.386
HF/SDD LEVEL												
−2.6752	8.0650	2.6752	−8.0650	10.7401	5.3701	0.1862	−2.694	2.6949	0.6762	1.4789	3.4542	−153264.624
M062X/3–21 g LEVEL												
−5.7661	0.0476	5.7661	−0.0476	5.8138	2.9069	0.3440	2.859	−2.8593	1.4062	0.7111	3.8614	−154198.850
M062X/6–31 g LEVEL												
−5.9014	0.2283	5.9014	−0.2283	6.1297	3.0648	0.3263	2.836	−2.8365	1.3126	0.7618	3.9808	−7422.930
M062X/SDD LEVEL												
−2.6379	2.9846	2.6379	−2.9846	5.6225	2.8112	0.3557	−0.173	0.1733	0.0053	187.12	1.1156	−153357.778

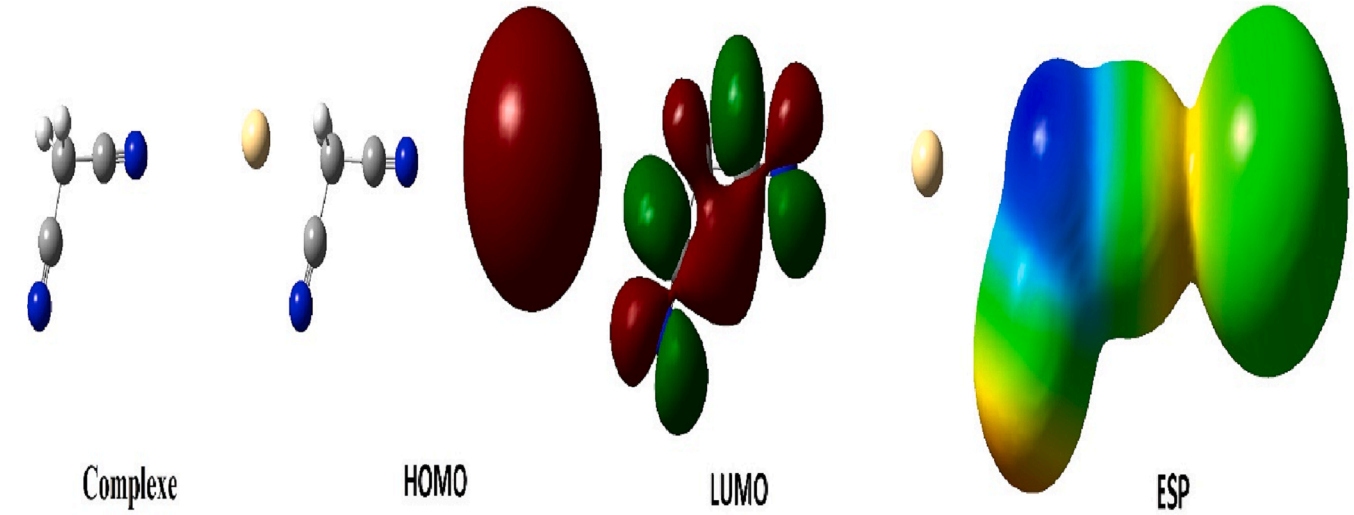

Fig.6. Optimize complex structure, HOMO, LUMO, and ESP.

Table 3
Fukui Functions value for a Nucleophilic and Electrophilic location.

Atoms	f^+	f^-	f^0
1C	−0.01	−0.01	−0.01
2C	−0.01	−0.01	−0.01
3C	0.06	0.05	0.05
4N	0.03	0.02	0.03
5N	−0.09	−0.07	−0.08
6Cd	1.00	1.00	1.00
7H	0.01	0.01	0.01
8H	0.01	0.01	0.01

However, the Fukui function also incorporates data on orbital relaxation or the alteration in orbital shape brought on by the addition and removal of electrons from the system and information regarding border molecular orbitals. The computations show that the 6Cd atom has the highest value followed by lowest 3C atom. The labelling of atoms in the metal complex is given in Fig.S6.

5.4. Nonlinear optical effects

To provide fundamental operations like optical modulation, frequency shifting, optical logic, optical switching, and optical memory for emerging technologies, NLO becomes essential. Such analyses are necessary for telecommunications, signal processing, and optical interconnects; many quanta chemical parameters are calculated when molecules' nonlinear optical effects (NLO) are examined [66]. Every determined metric provides crucial details about the molecules. These numerically measured characteristics, Polarizability (α) and hyperpolarizability (β) are estimated to forecast the nonlinear optical properties of materials. Polarizability and hyperpolarizability make up the two components of the dipole moment (μ).

Parameters for molecules. The parameters listed below can be used to compute the NLO characteristics of molecules:

$$\mu = \sqrt{(\mu_x^2 + \mu_y^2 + \mu_z^2)} \tag{1}$$

$$\alpha = 2^{-1/2}[(\alpha_{xx} - \alpha_{yy})^2 + (\alpha_{yy} - \alpha_{zz})^2 + (\alpha_{zz} - \alpha_{xx})^2 + 6\alpha_{xx}^2]^{1/2} \tag{2}$$

$$\alpha = \left(\frac{\alpha_{xx} + \alpha_{yy} + \alpha_{zz}}{3}\right) \tag{3}$$

$$\beta_{tot} = [(\beta_{xxx} + \beta_{xyy} + \beta_{xzz})^2 + (\beta_{yyy} + \beta_{yzz} + \beta_{yxx})^2 + (\beta_{zzz} + \beta_{zxx} + \beta_{zyy})^2]^{1/2} \tag{4}$$

The compounds' Polarizability (α_0) and hyperpolarizability (β_{tot}) values were computed. When converting these estimated parameters

into electrostatic units ($\alpha : 1a.u. = 0.148x10^{-24}esu$ and $\beta : 1a.u. = 8.639x10^{-33}esu$), the atomic unit (a.u.) is multiplied by constant values. As the dipole moment, linear Polarizability, polarizability anisotropy, and initial hyperpolarizability rise, so do the properties of NLOs. These characteristics, listed in Table 4, were computed using the HF/lanl2dz basis set for the metal complex.

5.5. Molecular docking

One of the standard methods used to compare the activities of metal complexes is a computer-based molecular docking study. It analyzes the interactions of molecules with various proteins in calculations. These interactions are generally chemical interactions. As these interactions increase, it is seen that the activities of metal complexes increase. $E_{Total\ Energy}$ value, one of the calculated parameters of the metal complex studied because of the calculations, is an important parameter used to compare the activities of the molecules. The molecular activity with the most negative numerical value of this parameter is known to be the highest. $E_{Total\ Energy}$ values of molecules calculated against various proteins are given in Table 5 [48]. The pictures of the interactions that occur due to the molecular docking calculations are presented in Fig.S7-S10.

5.6. Protein-ligand interaction profiler

Further, high-level computer-assisted protein–ligand interaction profiler (PLIP) analysis was performed to examine interactions in more detail. The numerical values of the interactions between the metal complex and the proteins were obtained in Table 6-7. As a result of the PLIP analysis, the metal complexes are given in Figs. 7–10 with their interaction with various proteins found in cancer proteins. In general, the interactions of the cadmium metal complex between cancer proteins are Hydrogen Bonds and Hydrophobic Interactions, shown in Figs. 7-10 and Tables 4-5. Concerning the subject line, a detailed discussion will be analyzed below: In Fig. 7, it is seen that the interaction between the metal complex and breast cancer protein creates Hydrophobic Interactions with the metal complex ILE, TRP, VAL, PRO, and ALA proteins. Fig. 8 shows that the interaction between metal complex and lung cancer protein creates Hydrophobic Interactions with metal complex TYR, LEU, PHE, and LEU proteins. Fig. 9 shows that the metal complex and liver cancer protein interaction creates Hydrophobic Interactions with the metal complex LEU, VAL, ILE, PHE, and LEU proteins. Similarly, Fig. 10 shows that the interaction between the metal complex and the colon cancer protein creates Hydrophobic Interactions with the metal complex LEU, VAL, ALA, and PHE proteins. In addition, in Fig. 7, hydrogen bonding occurs between the metal complex and breast cancer protein and between LYS and VAL proteins and the metal complex.

6. Photodynamic antifungal chemotherapy

Antifungal activity of the complex (**C1**), TCM, and $Cd(OAc)_2{\cdot}2H_2O$ against Aspergillus niger and Candida Albicans was studied by the well diffusion method, and here photodynamic therapy (PDT) studies of the samples were conducted after irradiating the sample for 2 h using a Newport Xenon arc lamp of 300 W. The time for irradiation was optimized to be 2 h as there was no observed increase in the antifungal activity after 2 h. The sample after irradiation is marked as **C1***, TCM*, and $Cd(OAc)_2{\cdot}2H_2O$*, and DMSO is the negative control. The results are shown in Fig.S11 and zones of inhibition are noted in Table 8. Again, the micro broth dilution method determined the minimum inhibitory concentration (MIC) against each strain for the irradiated samples. MIC is the minimum concentration of an antifungal that visibly inhibits the growth of the microbe. The experiments were performed at five different concentrations – 2 μg/mL, 4 μg/mL, 8 μg/mL, 16 μg/mL, and 32 μg/mL to determine the MIC. All the measurements were done in six replicates, and one-way ANOVA was carried out on all the results. Duncan's multiple range test (DMRT) is used as the post hoc test at a significance level of p B 0.05 using SPSS 16.0 software in the present statistics. All the compounds were active against the two specified strains in this experiment. **C1** exhibited considerable activity against the two microbes, and their inhibition zones were similar against each strain. Complex, TCM and $Cd(OAc)_2.2H_2O$ shows significant activity against both fungi. Based on the experiment, it was observed that the activity increased when the sample was irradiated. The irradiated samples, **C1***, TCM*, and $Cd(OAc)_2{\cdot}2H_2O$*, have an increase in zone diameter of about 1–1.5 mm against each strain. The result mentioned above indicates the success of our presently modified system in photodynamic therapy (PDT) or, more

Table 4
NLO parameters value.

a.u.	esu	a.u.	esu
85.1287	1.2599×10^{-23}	65.7270	5.679×10^{-28}
−4.9958	-7.3938×10^{-25}	93.5166	8.081×10^{-28}
130.1136	1.92568×10^{-23}	−104.4546	-9.026×10^{-28}
0.0000	$0.000 \times 10^{+00}$	1095.7993	9.469×10^{-27}
0.0000	$0.000 \times 10^{+00}$	0.0000	$0.000 \times 10^{+00}$
92.9972	1.37636×10^{-23}	0.0000	$0.000 \times 10^{+00}$
70.0822	1.03722×10^{-23}	0.0000	$0.000 \times 10^{+00}$
−2.6694		−1048.2271	-9.058×10^{-27}
4.7573		69.6839	6.021×10^{-28}
0.0000		1503.9363	1.300×10^{-26}
5.4551			

Table 5
$E_{Total\ energy}$ value of Molecular docking parameter for metal complex.

Docking parameters	Metal complex
Breast cancer	−215.39
Lung cancer	−242.95
Liver cancer	−133.73
Prostate cancer	−148.25

Table 6
Hydrophobic Interactions of protein and metal complex.

Index	Residue	AA	Distance	Ligand atom	Protein atom
Breast cancer - metal complex					
1	1707X	ILE	3.25	1969	544
2	1712X	TRP	2.76	1964	587
3	1713X	VAL	3.05	1969	599
4	1749X	PRO	3.26	1969	915
5	1752X	ALA	3.99	1969	934
Lung cancer - metal complex					
1	36A	TYR	3.44	1286	539
2	39A	LEU	2.83	1291	585
3	45A	PHE	2.53	1291	682
4	71A	LEU	3.08	1286	1117
Liver cancer - metal complex					
1	924A	LEU	3.21	3119	1061
2	1012A	VAL	2.55	3119	1425
3	1034A	ILE	3.22	3119	1654
4	1091A	PHE	2.68	3124	2222
5	1094A	LEU	3.56	3124	2244
6	1094A	LEU	3.61	3119	2246
7	1095A	LEU	2.90	3124	2255
Colon cancer - metal complex					
1	237A	LEU	2.57	2474	785
2	238A	VAL	3.71	2479	795
3	241A	ALA	2.85	2479	829
4	334A	LEU	3.91	2479	1556
5	338A	LEU	3.91	2474	1598
6	373A	PHE	3.48	2479	1876
7	398A	LEU	2.90	2479	2099

In Table 6: ALA: Alanine, ILE: Isolosine, LEU: Leucine, PRO: Proline, TRP: Tryptophan, TYR: Tyrosine, Val: Valine.

Table 7
Hydrogen Bonds of protein and metal complex.

Index	Residue	AA	Distance H-A	Distance D-A	Donor angel	Protein donor?	Side chain	Donor Atom	Acceptor Atom
Breast cancer -metal complex									
1	1711X	LYS	1.61	2.30	119.71	X	X	1968 [N3]	567 [O2]
2	1713X	VAL	2.28	3.14	144.18	√	X	593 [Nam]	1968 [N3]

In Table 7: LYS: Lizin, Val: Valine.

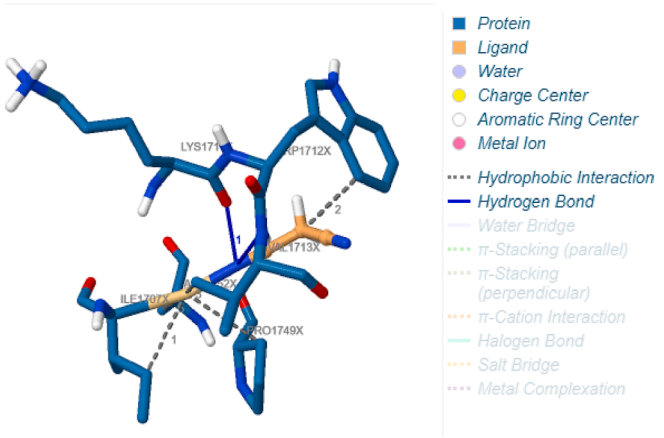

Fig.7. Representation of the interaction of metal complex with staphylococcus aureus.

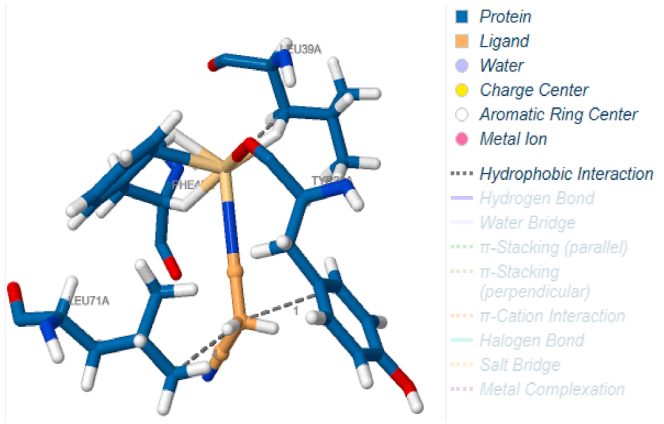

Fig.8. Representation of the interaction of metal complex with Escherichia coli.

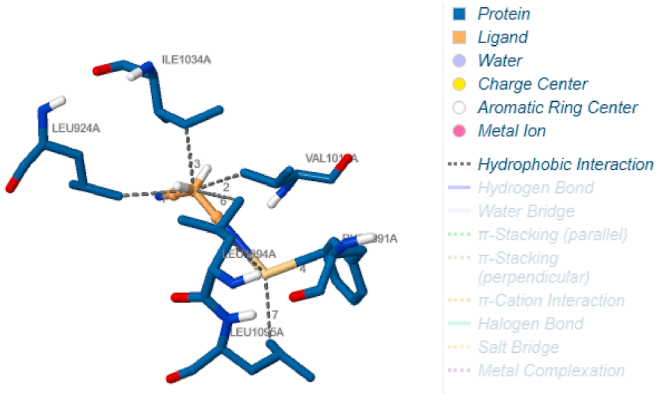

Fig.9. Representation of the interaction of metal complex with Escherichia coli.

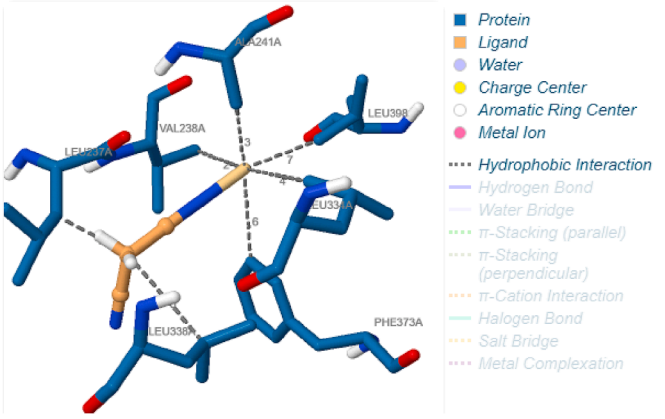

Fig.10. Representation of the interaction of metal complex with Escherichia coli.

specifically, photodynamic antifungal chemotherapy (PACT). The irradiated samples (**C1***,* TCM*, and $Cd(OAc)_2{\cdot}2H_2O$*) showed remarkable activity against A. niger (Table 8). The research of photodynamic antifungal chemotherapy is a growing field that involves biological coordination chemistry due to its significance in everyday life. Scientists worldwide are dedicating their research efforts to PACT. We have compared our findings on PACT in the coordination complex community to previous studies. As reported in the literature, our synthesized complex PACT results are comparable to those of Ru, Cu, Pd, Ni, and Zn coordination complexes [67–71]. Indeed, we have first submitted a new cadmium coordination polymer with TCM building blocks for PACT investigation.

6.1. *Mechanism of fungal inhibition*

It is crucial to investigate the fundamental mechanism that promotes PACT thoroughly. Two factors, membrane disruption and cell cycle arrest, are the most proposed mechanisms of the antifungal activity of the cadmium complex [72,73]. Reactive oxygen species (ROS) dependent fungal cell death can also be a favourable reason [74]. ROS compounds could be the predominant mechanism of fungal inhibition in PDT. The use of PDT in medicine has opened new treatment options. It involves using a photosensitizing drug (a photosensitizer or PS) to treat different diseases. When exposed to a specific wavelength of light, these drugs produce oxygen-free radicals that can harm nearby living cells. After excitation, the PS electrons in the excited singlet state undergo intersystem crossing (ISC) to the triplet state. This triplet state can react differently with the biomolecules (Type I or II). The above discussion is depicted in Fig.S12. According to Fig.S12, Type I reaction involves electron transfer from triplet-state PS to an organic substrate within cells, producing free radicals. These free radicals interact with oxygen at the molecular level, producing reactive oxygen species (ROS) such as O_2^-, $OH^{\cdot}$, and H_2O_2, which can harm living cells. During the Type II reaction, the excited PS transfers energy to the ground-state molecular oxygen. It produces singlet oxygen, which can interact with various molecules within the cell, forming oxidized products. MIC values for each strain are determined and noted in Table 9. In our experiment, the MIC value determined for each strain in PDT is 2 μg/mL.

Table 8
Antifungal zones of inhibition in PACT (Photodynamic antimicrobial chemotherapy).

Fungal strain/sample	Zone of inhibition ± standard deviation (mm)					
	C1	**C1***	**TCM**	**TCM***	**$Cd(OAc)_2{\cdot}2H_2O$**	**$Cd(OAc)_2{\cdot}2H_2O$***
A. niger	3.00 ± 1.67	4.02 ± 1.07[a]	1.30 ± 0.87	2.33 ± 2.81[a]	5.00. ± 1.72	6.00. ± 0.75[a]
C. Albicans	3.00 ± 0.98	4.31 ± 0.19[a]	4.00 ± 1.57	5.06 ± 1.07[a]	3.90. ± 0.82	5.00. ± 1.12[a]
PB 0.05F = 435.949						

'*' Irradiated sample. The significance level 'a' predicted by DMRT says that the two results are statistically equivalent.

Table 9
Antifungal zones of inhibition and MIC values C1*in PACT (Photodynamic antimicrobial chemotherapy).

Fungal strain	Zone of inhibition ± standard deviation (mm)	MIC determination					MIC (μg/mL)
		2 μg/mL	4 μg/mL	8 μg/mL	16 μg/mL	32 μg/mL	
A. niger	4.02 ± 1.07[a]						2
C. Albicans	4.31 ± 0.19 [a]						2

The '-' sign against each concentration in Table 8 denotes the inhibition of microbial growth at the particular concentration.

6.2. Fungal Time-kill kinetics study

Time-kill kinetic study exhibits basic pharmacodynamic information on the relationship between the synthesized complex and the growth of microorganisms. This test thereby contributes to a better understanding of the current and future application of the compound against the diseases caused by the respective fungal. Time-kill kinetics study for the complex **(C1)** against *A. niger* and the complex against *C. Albicans* is shown in Fig.S13. It offers the negative control represented by the standard growth curve of *A. niger* and *C. Albicans*. We conducted time-kill studies to explore the kinetics of the complex in killing *A. niger and C. Albicans* at a range of concentrations. As shown in Fig.S13, the complex could thoroughly eliminate *A. niger* within 60 min at 48 μg/mL concentrations. Only 30 min was required at the concentration of 48 μg/mL to eradicate *C. Albicans*, which was faster than *A. niger*. This observation showed that the complex was effective in killing *A. niger and C. Albicans*, where the lag period remained for 1 h. After that, the exponential growth or the log phase occurred, followed by a stationary phase. In the case of complex microorganisms, a very short exponential growth phase was observed compared to the untreated control. For the complex, 40th minutes of incubation, the bacterial CFU enters the declining phase, i.e., the death phase. Thus, this observation revealed that the complex showed promising fungal activities.

7. Conclusions

To summarize, this research focuses on photodynamic antifungal chemotherapy and in-depth analysis of a Cd(II)-TCM coordination polymer using DFT exploration. The article also outlines the complex's synthesis, structural characterization, and crystal structure validation. X-ray structure explores Cd(II) centres that assume octahedral geometry and are coordinated by six N atoms from six TCM. The topology analysis shows an sqc8 topology with Cd(II) in the nodes where the TCM connectors form edges. The crystal packing consists of unique nitrile···nitrile interactions at 3.276 Å. Remarkably, HSA delineated the supramolecular exchanges where the Cd···N contact (35.1%) is the prevailing crystal packing and C···C and N···N contacts also contribute 21.2% and 20.6%, respectively. The complex DFT optimization was made in B3LYP, HF, and M06-2x methods using the 3–21 g, lanl2dz, and sto-3 g level of basis sets. The concepts of the HOMO-LUMO energy gap and ESP are essential in understanding chemical reactivity and electron density. The Fukui function values (f_x^+, f_x, *and* f^0) help to identify the areas of electrophiles (E+) and nucleophiles (Nu^-). NLO parameters can provide insight into optical properties. Here MD and PLIP result in an adequate understanding of complex biological interactions. This article focuses on photodynamic antifungal therapy and its efficacy against antibiotic-resistant strains. The results report compares complex, TCM, and metal salts in this therapy with MIC values. The MIC for two strains was found to be 2.5 μg/mL. The research outcome suggests the complex can be developed as an antifungal agent. The perspective of MD and PLIP experiments will be an essential reference for upcoming in vitro and in vivo studies. Additionally, members of the computational chemistry community have expressed interest in presenting DFT results in a way that allows for further research with TCM building blocks.

CRediT authorship contribution statement

Dhrubajyoti Majumdar: Project administration, Data curation, Conceptualization, Methodology, Formal analysis, Investigation, Software, Visualization, Resources, Supervision, Validation, Writing - original draft, Writing - review & editing. **Jessica Elizabeth Philip:** Data curation, Formal analysis, Software, Visualization. **Burak Tüzün:** Data curation, Formal analysis, Software, Visualization. **Sourav Roy:** Data curation, Formal analysis, Software, Visualization.

Declaration of Competing Interest

The authors declare that they have no known competing financial interests or personal relationships that could have appeared to influence the work reported in this paper.

Data availability

The data that has been used is confidential.

Acknowledgments

This research has yet to receive specific funding from any funding agency in the public, commercial, or non-profit sectors. All authors thank the Central Laboratory of Tamralipta Mahavidyalaya, Tamluk-721636, West Bengal, India, funded by the DST-FIST project (Level-0) under the Department of Science and Technology, Govt. from India. All manuscript authors carefully read and approved the final version before submission.

Appendix A. Supplementary material

CCDC 2195419 contains the supplementary crystallographic data for the complex. These data can be obtained free of charge via http://www.ccdc.cam.ac.uk/conts/retrieving.html, or from the Cambridge Crystallographic Data Centre, 12 Union Road, Cambridge CB2 1EZ, UK; fax: (+44) 1223-336-033; or e-mail: deposit@ccdc.cam.ac.uk. Supplementary data to this article can be found online at https://doi.org/10.1016/j.inoche.2023.111057.

References

[1] T.K. Maji, K. Uemura, H.C. Chang, R. Matsuda, S. Kitagawa, Angew. Chem. Int. Ed. 43 (2004) 3269–3272.

[2] T. Shiga, H. Okewa, S. Kitagawa, M. Ohba, J. Am. Chem. Soc. 128 (2006) 16426–16427.
[3] B.F. Abrahams, S.R. Batten, B.F. Hoskins, R. Robson, Inorg. Chem. 42 (2003) 2654–2664.
[4] J. Kohout, L. Jäger, M. Hvastijová, J. Kožíšek, J. Coord. Chem. 51 (2000) 169–218.
[5] T. Linkowski, J.L. Burmeister, Inorg. Chim. Acta. 17 (1976) 117–120.
[6] Chemistry of Pseudohalides, in: A. M. Golub. H. Kohlers, and V. V. Skopenko (Eds.) Topics in Inorganic and General Chemistry (Elsevier), 21 (1987) 413-454.
[7] J. Luo, X.-R. Zhang, E.-Q. Gao, W.-Q. Dai, L.-L. Cui, B.-S. Liu, Chin. J. Chem. 26 (2008) 835–841.
[8] C. Yuste, D. Armentano, N. Marino, L. Cãnadillas-Delgado, F.S. Delgado, C. Ruiz-Pérez, D.P. Rillema, F. Lloret, M. Julve, Dalton Trans. (2008) 1583–1596.
[9] L.-Y. Zhang, L.-X. Shi, Z.-N. Chen, Inorg Chem. 42 (2003) 633–640.
[10] L.F. Jones, L.O. Dea, D.A. Offermann, P. Jensen, B. Moubaraki, K.S. Murray, Polyhedron 25 (2006) 360–372.
[11] V.M. Deflon, C.C. de Sousa Lopes, K.E. Bessler, L.L. Romualdob, E. Niquet, Z. Naturforsch. 61b (2006) 33–36.
[12] X. Zhang, L.Y. Zhang, L.X. Shi, Z.N. Chen, Inorg. Chem. Commun. 12 (2009) 758–760.
[13] A. Masoudiasl, M. Montazerozohori, S. Joohari, L. Taghizadeh, G. Mahmoudi, A. Assoud, J. Ultsonch. 52 (2019) 244–256.
[14] S.A. Mousavi, M. Montazerozohori, R. Naghiha, A. Masoudias, S. Mojahedi, T. h. Doert, Appl. Organomet. Chem. 34 (2020) e5550.
[15] D.J. Majumdar, B. Tüzün, T.K. Pal, S. Das, J. Kalipada Bankura, Inorg. Organomet. Polym. 32 (2022) 1159–1176.
[16] D.J. Majumdar, B. Tüzün, T.K. Pal, R.V. Saini, K. Bankura, D. Mishra, Polyhedron 210 (2021), 115504.
[17] P. Fuentealba, P. Pérez, R. Contreras, J. Chem. Phys. 113 (7) (2000) 2544–2551.
[18] L. H. Lee, Applications of the hard-soft acid-base (HSAB) principle to solid adhesion and surface tribointeractions, in: Surfactants and macromolecules: self-assembly at interfaces and in bulk, (1990) 337-344.
[19] L.H. Lee, J. Adhesion 36 (1) (1991) 39–54.
[20] Y. Li, J.N. Evans, J. Am. Chem. Soc. 117 (29) (1995) 7756–7759.
[21] S. Krishnamurty, R.K. Roy, R. Vetrivel, S. Iwata, S. Pal, J. Phys. Chem A. 101 (39) (1997) 7253–7257.
[22] A.D. Becke, J. Chem. Phys. 96 (3) (1992) 2155–2160.
[23] D. Vautherin, D.T. Brink, Phys. Rev. C. 5 (3) (1972) 626.
[24] E.G. Hohenstein, S.T. Chill, C.D. Sherrill, J. Chem. Theory Computation 4 (12) (2008) 1996–2000.
[25] M. Montazerozohori, S. Zahedi, M. Nasr-Esfahani, A. Naghiha, J. Ind. Eng. Chem. 20 (2014) 2463–2470.
[26] M. Montazerozohori, S.A. Musavi, A. Masoudiasl, A. Naghiha, M. Dusek, M. Kucerakova, Spectrochim Acta Part A 137 (2015) 389–396.
[27] R.S. Williams, R. Green, J.N. Glover, Nat. Struct. Biol. 8 (10) (2001) 838–842.
[28] H. Li, K.L. Fung, D.Y.S.S. Chung, Y.P. Ching, I.O.L. Ng, H. Sun, Proteins: Struct. Function Bioinformatics 67 (4) (2007) 1154–1166.
[29] K. Okamoto, M. Ikemori-Kawada, A. Jestel, K. Von König, Y. Funahashi, T. Matsushima, J. Matsui, ACS Med. Chem. Lett. 6 (1) (2015) 89–94.
[30] A.A. Marusiak, N.L. Stephenson, H. Baik, E.W. Trotter, Y. Li, K. Blyth, J. Brognard, Cancer research 76 (3) (2016) 724–735.
[31] J. Avijita, S.J. Brenda, J.B. Karen, Inorg. Chim. Acta. 538 (2022), 120996.
[32] J. Karges, H. Chao, G.J. Gasser, J. Biol Inorg Chem. 25 (2020) 1035–1050.
[33] M. Susan, L.C. Katsuya, Y. Huimin, R. John, K. Prathyusha, G. Shashi, P. T. Randolph, L. Lothar, G.C. Colin, A.M. Sherri, Chem Rev. 119 (2) (2019) 797–828.
[34] C.P. Stefania, V.A. Thiago, M.S. Janio, B.D. Laura, A.I. Bernardo, Photodiagnosis Photodyn. Ther. 36 (2021), 102550.
[35] K.M. Luke, V.S. Igor, B. Elizabeth, B. Mickaële, G. Véronique, W. Gareth, A. W. Julia, E.B. Helen, Chem. Eur. J. 23 (2007) 234.
[36] L. Yi, L. Li-Ming, C. Yong, L. You-Kun, Experimental and Therapeutic Medicine 12 (2016) 23–27.
[37] K. Johannes Karges, Angewandte Chemie. 61 (2022) 5.
[38] W. Yanping, L. Shumeng, C. Yuncong, H. Weijiang, G. Zijian, Chem. Sci. 13 (2022) 5085–5106.
[39] G.M. Sheldrick, SADABS, a software for empirical absorption correction, Ver.2.05; University of Göttingen: Göttingen, Germany, 2002.
[40] SMART & SAINT Software Reference manuals Version 6.45; Bruker Analytical X-ray Systems, Inc.: Madison, WI, 2003.
[41] SHELXTL Reference Manual Ver. 6.1; Bruker Analytical X-ray Systems, Inc.: Madison, WI, 2000.
[42] G.M. Sheldrick, SHELXTL, a software for empirical absorption correction Ver.6.12; Bruker AXS Inc.: WI. Madison, 2001.
[43] O.V. Dolomanov, L.J. Bourhis, R.J. Gildea, J.A.K. Howard, H. Puschmann, OLEX2, OLEX2: a complete structure solution, refinement, and analysis program, J. Appl. Crystallog. 42 (2009) 339–341.
[44] M. Chalkha, A.A. Hassani, A. Nakkabi, B. Tüzün, M. Bakhouch, A.T. Benjelloun, M. El Yazidi, J. Mol. Struc. (2022), 134255.
[45] R. Dennington, T.A. Keith, J.M. Millam, GaussView 6.0. 16. Semichem Inc.: Shawnee Mission, KS, USA, 2016.
[46] Gaussian 16, Revision C.01, M. J. Frisch, G. W. Trucks, H. B. Schlegel, G. E. Scuseria, M. A. Robb, J. R. Cheeseman, G. Scalmani, V. Barone, G. A. Petersson, H. Nakatsuji, X. Li, M. Caricato, A. V. Marenich, J. Bloino, B. G. Janesko, R. Gomperts, B. Mennucci, H. P. Hratchian, J. V. Ortiz, A. F. Izmaylov, J. L. Sonnenberg, D. Williams-Young, F. Ding, F. Lipparini, F. Egidi, J. Goings, B. Peng, A. Petrone, T. Henderson, D. Ranasinghe, V. G. Zakrzewski, J. Gao, N. Rega, G. Zheng, W. Liang, M. Hada, M. Ehara, K. Toyota, R. Fukuda, J. Hasegawa, M. Ishida, T. Nakajima, Y. Honda, O. Kitao, H. Nakai, T. Vreven, K. Throssell, J. A. Montgomery, Jr., J. E. Peralta, F. Ogliaro, M. J. Bearpark, J. J. Heyd, E. N. Brothers, K. N. Kudin, V. N. Staroverov, T. A. Keith, R. Kobayashi, J. Normand, K. Raghavachari, A. P. Rendell, J. C. Burant, S. S. Iyengar, J. Tomasi, M. Cossi, J. M. Millam, M. Klene, C. Adamo, R. Cammi, J. W. Ochterski, R. L. Martin, K. Morokuma, O. Farkas, J. B. Foresman, D. J. Fox, Gaussian, Inc., Wallingford CT, 2016.
[47] A. Tas, B. Tüzün, A.N. Khalilov, P. Taslimi, T. Ağbektas, N.K. Cakmak, J. Mol. Struc. (2022), 134282.
[48] F. Türkan, P. Taslimi, B. Cabir, M.S. Ağırtaş, Y. Erden, H.U. Celebioglu, I. Gulcin, Polycyclic Aromatic Compounds 42 (7) (2022) 4475–4486.
[49] D. Ritchie, and T. Orpailleur, Hex 8.0. 0 User Manual. Protein Docking Using Spherical Polar Fourier Correlations Copyright, 2013.
[50] S. Salentin, S. Schreiber, V.J. Haupt, M.F. Adasme, M. Schroeder, Nucleic acids Res. 43 (W1) (2015) W443–W447.
[51] M.F. Adasme, K.L. Linnemann, S.N. Bolz, F. Kaiser, S. Salentin, V.J. Haupt, M. Schroeder, Nucleic Acids Res. 49 (W1) (2021) W530–W534.
[52] M.A. Spackman, D. Jayatilaka, CrystEngComm. 11 (2009) 19–32.
[53] F.L. Hirshfeld, Theor. Chem. Acta. 44 (1977) 129–135.
[54] H.F. Clausen, M.S. Chevallier, M.A. Spackman, B.B. Iversen, New J. Chem. 34 (2010) 193–199.
[55] A.L. Rohi, M. Moret, W. Kaminsky, K. Claborn, J.J. McKinnon, B. Kahr, Cryst. Growth Des. 8 (2008) 4517–4525.
[56] A. Parkin, G. Barr, W. Dong, C.J. Gilmore, D. Jayatilaka, J.J. McKinnon, M. A. Spackman, C.C. Wilson, CrystEngComm. 9 (2007) 648–652.
[57] M.A. Spackman, J.J. McKinnon, CrystEngComm. 4 (2002) 378–392.
[58] N.N. Samuel, O. Lucy, M. Eric, N. Margaret, Adv. Chem. (2018) 2598062.
[59] (a) B. Dutta, S. Paul, S. Halder, Heliyon (2023) e13504;
(b) D. Dutta, P. Sharma, A. Frontera, A. Gogoi, A.K. Verma, D. Dutta, B. Sarma, M. K. Bhattacharyya, New J. Chem. 44 (2020) 20021–20038;
(c) A. Poulin, M. Kubickia, C. Lecomte, Acta Cryst. B 70 (2014) 973–982;
(d) S.R. Batten, B.F. Hoskins, B. Moubaraki, K.S. Murray, R. Robson, J. Chem. Soc., Dalton Trans. (1999) 2977–2986.
[60] M. Tapera, H. Kekeçmuhammed, B. Tüzün, E. Sarıpınar, U.M. Koçyiğit, E. Yıldırım, Y. Zorlu, J. Mol. Struc. 1269 (2022), 133816.
[61] M.S. Çelik, S.A. Çetinus, A.F. Yenidünya, S. Çetinkaya, B. Tüzün, J. Mol. Struc. 1272 (2023), 134158.
[62] U.M. Koçyiğit, M. Doğan, H. Muğlu, P. Taslimi, B. Tüzün, H. Yakan, I. Gülçin, J. Mol. Struc. (2022, 1264,), 133249.
[63] A.K. Pandey, D.V. Shukla, V.N. Mishra, V. Singh, O.P. Yadav, A. Dwivedi, J. Ind. Chem. Soc. 99 (4) (2022), 100396.
[64] R. Pucci, G.G.N. Angilella, Foundations of Chemistry (2022) 1–13.
[65] A. Morales-Bayuelo, J. Sánchez-Márquez, J. Mol. Model. 28 (5) (2022) 1–13.
[66] S.R. Marder, Chem. Commun. 2 (2006) 131–134.
[67] P. Sen, T. Nyokong, J. Mol. Struc. 1232 (2021), 130012.
[68] R.-K. Lin, C.-I. Chiu, C.-H. Hsu, Y.-J. Lai, P. Venkatesan, P.-H. Huang, P.-S. Lai, C.-C. Lin, Chem. Eur. J. 24 (2018) 1–11.
[69] P. Sen, T. Nyokong, Polyhedron 173 (2019), 114135.
[70] M.A. Malik, O.A. Dar, P. Gull, M.Y. Wani, A.A. Hashmi, Med. Chem. Commun. 9 (2018) 409–436.
[71] M.A. Tiburcio, A.R. Rocha, R.A. Romano, N.M. Inada, V.S. Bagnato, R.M. Carlos, H. H. Buzzá, J. Photobiol. B. 229 (2022), 112414.
[72] M. Kumari, V.P. Giri, S. Pandey, M. Kumar, R. Katiyar, C. Nautiyal, A. Mishra, Pestic Biochem Physiol. 157 (2019) 45–52.
[73] K. Kim, W.S. Sung, B.K. Suh, S. Moon, J. Choi, J.G. Kim, D.G. Lee, Biometals. 22 (2009) 235–242.
[74] M.I. Das, R. Khan, S.K. Jayabalan, S. Behera, S.I. Yun, S.K. Tripathy, A. Mishra, Sci. Rep. 6 (2016) 36403.